UC Davis
UC Davis Previously Published Works

Title
Electrodeposition of Ni and Te-doped Cobalt Triantimonide in Citrate Solutions

Authors
Vidu, Ruxandra
Perez-Page, Maria
Quach, Dat V
et al.

Peer reviewed

Electrodeposition of Ni and Te−Doped Cobalt Triantimonide in Citrate Solutions

Ruxandra Vidu,*[a] Maria Perez-Page,[a] Dat V. Quach,[a] Xinyi Y. Chen,[a] and Pieter Stroeve[a]

Abstract: Skutterudite compounds form a new class of potential candidates for thermoelectric applications. Cobalt triantimonide ($CoSb_3$) shows good thermoelectric properties at medium and high temperatures. Doping this system with substitution elements, for either Co or Sb or both, may result in an increase of the thermoelectric figure of merit (ZT). This work focused on the electrochemical doping and characterization of films and nanowires of Co-Sb system in citrate solutions using gold-coated PCTE templates. The electrodeposition was performed on gold surface that was pre-treated electrochemically to ensure reproducible results. The electrochemical treatment acted as an annealing process for the surface, which resulted in an increase in Au(111) as demonstrated by XRD. Detailed electrochemical studies including deposition-stripping experiments was performed in order to develop a better understanding of the co-deposition kinetics and a better control over the composition of doped Co-Sb system. Scanning electron microscopy (SEM/EDS) helped study the morphology and the composition of the doped and undoped Co-Sb system. Co-deposition of Co-Sb showed that the amount of Co is higher in nanowires than in film or mushroom caps due to the slow Sb deposition rate dictated by slow Sb(III) complex diffusion. Doped nanowires have been also obtained. Both Ni and Te electrochemical doping of the Co-Sb system affected the composition of the deposit but there was no effect on nanowire morphology.

Keywords: Skutterudites · Thermoelectrics · $CoSb_3$ · Electrochemical Doping · Nanowires

1. Introduction

Over the past decade, there has been a great interest in research on alternative and renewable energy sources, which is driven by the high price of crude oil and global efforts to reduce carbon dioxide emission. Thermoelectric materials may play an important role in the global search for sustainable energy solutions. Thermoelectrics directly convert heat to electricity based on the Seebeck effect. In addition to their applications as thermoelectric generators, thermoelectric devices can be used as electronic refrigeration for the ever smaller computer chips and circuits boards [1].

Cobalt triantimonide, $CoSb_3$, is a compound with a skutterudite structure which has been identified as a potential new material for thermoelectric materials at intermediary temperatures (400–700 °C). The efficiency of a thermoelectric material is determined by its dimensionless thermoelectric figure of merit ZT that can be expressed by eq. 1 [1b, 2]:

$$ZT = \frac{S^2 \cdot \sigma \cdot T}{\kappa} \qquad (1)$$

where, S is the Seebeck coefficient, σ electrical conductivity, κ thermal conductivity and T absolute temperature. Thermal conductivity property is a result of both electronic (λ_E) and lattice conductivity (λ_L) contributions. A good thermoelectric material should possess a large power factor ($S^2\sigma$) and a low thermal conductivity.

Skutterudites, especially of n-type conductivity, are of special interest due to their excellent electrical transport properties and large Seebeck coefficient. Unfortunately, the thermal conductivities of the binary skutterudites are too large for thermoelectric applications. In order to optimize conflicting properties such as those required by thermoelectric materials, a variety of compositional, structural and dimensional modifications are needed. Slack [3] suggested that the figure of a merit of a thermoelectric materials can be improved if the two conductivities are independently adjusted. This is known as the phonon-glass electron-crystal (PGEC) model, in which the thermoelectric material should possess both a *crystalline structure* to guarantee a good electric conductivity with little electron scattering and a *glass structure* to decrease the thermal conduction by inducing a high degree of phonon scattering.

Besides having an excellent power factor, $CoSb_3$ has a unit cell with two cage-like voids formed by the Sb atoms, which offers the necessary space to introduce additional scatters to improve the thermoelectric figure of merit. As shown by eq. 1, thermoelectric properties can be improved by increasing the electrical conductivity while reducing the thermal conductivity of a given material system. This is an excellent example of the PGEC concept in which phonon scattering centers can be introduced in the unit cell to lower the lattice thermal conduc-
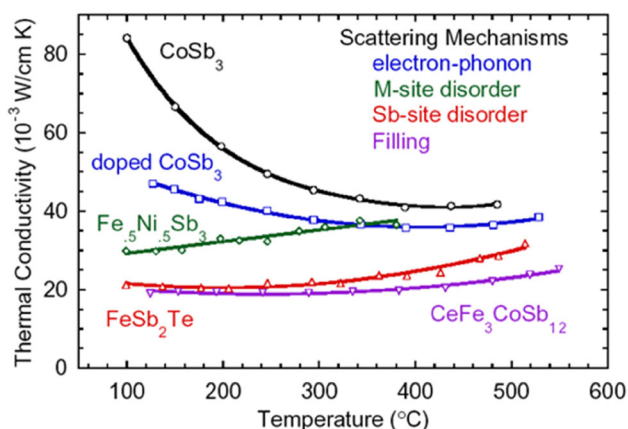
These are not the final page numbers! ↗↗

Fig. 1.   Influence of doping scattering mechanism on the thermal conductivity of CoSb$_3$-type skutterudites [9]

tivity. Most of today's research focuses on reducing lattice thermal conductivity by introducing large heavy atoms into the skutterudite structure [2,4], which can be achieved by doping.

In the following, the importance of doping associated with small dimension is briefly discussed.

The effects of doping with various donor impurities on the thermoelectric properties of polycrystalline CoSb$_3$ have been extensively studied [5]. The analysis of the transport properties suggests that the electronic properties depend strongly on both the donor impurities (either fillers or dopants) and the carrier concentration, which control not only the electronic transport properties but also the scattering mechanisms of phonons in heavily doped n-type CoSb$_3$. The substitution of Co or Sb in CoSb$_3$ with different dopants can influence the electronic structure and electrical properties, in particular by changing the carrier masses. Furthermore, doping affects the lattice thermal conductivity due to phonon scattering on impurities.

Dopants such as Ni, to replace Co, and Te, to replace Sb, can be used to further optimize the electrical conductivity and effectively scatter phonons [2,4b,6]. Figure 1 shows the decrease of thermal conductivity in skutterudites due to various scattering mechanisms. A total substitution of Co with Fe and Ni in a proportion of Fe:Ni = 1:1 results in a decrease of the thermal conductivity of about 2.7 times, while the substitution of Sb with Te results in a decrease of the thermal conductivity of about 4 times. Ni affects the electronic structure and electrical properties of skutterudites. In addition, Ni doping along with other fillers may be responsible for the existence of an additional band explained by the two-band theory [7]. This band shows up across the gap that touches the conduction band at the minimum point [8] and it is dues to the hybridization of the transition elements. In general, heavy doping has a great influence on the band structure due to the changes in the lattice constant and/or in the electronic bonding properties, resulting in noticeable changes in the thermoelectric properties.

Electronic transport and thermoelectric properties are strongly influenced by the addition of Ni impurities in Co [10]. Doping CoSb$_3$ mainly affects the lattice thermal conductivity. The dopant element introduces phonon scattering points that decrease the lattice thermal conductivity. Ur *et al.* [11] have shown that homogeneous hot-pressed Co$_{1-x}$Ni$_x$Sb$_3$ can be obtained by hot-pressing techniques when x = 0 to 0.1. For Ni content higher than 0.2, the compound decomposed to (Co, Ni)Sb$_2$ and Sb. Hall and Seebeck coefficients confirmed that Ni dopant generated more electrons [10]. As the doping element increases, the carrier concentration increases resulting in n-type conduction for Ni-doped CoSb$_3$. Unlike the carrier concentration, the carrier mobility decreased with the increase of Ni content, which demonstrates the role of Ni as an impurity scattering point in the electronic structure of CoSb$_3$. A reduction in carrier mobility by the decrease in the electron mean free path induced by the donor scatters is overcome by the increase in carrier concentrations, which overall decreases the electric resistivity and Seebeck coefficient. Ni doping introduces impurity scattering centers in both electronic and photonic structures of CoSb$_3$. As the carrier concentration increased, the thermal conductivity decreased. The dominant effect of Ni doping was observed on the lattice contribution (λ_L) to the total thermal conductivity with little effect on the electronic thermal conductivity (λ_E) [11].

Unlike Ni, doping CoSb$_3$ with Te increases electric conductivity, and has relatively smaller impact on thermal conductivity and Seebeck coefficient, thus improving the thermoelectric figure of merit ZT of the material [4b,6c]. Wojciechowski *et al.* [12] studied the structural and electron transport properties of and Te-doped CoSb$_3$ skutterudites. Calculations of the electrical and thermal conductivities and Seebeck coefficient as a function of composition and temperature showed that doping CoSb$_3$ with Te affects the density of electronic states. The solubility of Te in the CoSb$_3$ structure is very small, i.e. about 1.5 at. % [4b], where the Te atoms take the Sb sites in the CoSb$_3$ structure.

The substitution of antimony by tellurium and cobalt by nickel can influence the electronic and electrical properties of the material. In a different approach, thermoelectric properties can also be improved by low dimensional structures (thin films, nanowires and quantum dots) as demonstrated by theoretical works [13] and experimental results on Si nanowires [14].

Various techniques have been applied to synthesize nanostructured thermoelectric materials such as molecular beam epitaxy (MBE), vapor-liquid-solid growth process, chemical vapor deposition (CVD), hydrothermal processes, pulsed laser deposition [15], DC magnetron sputtering [16] and electrodeposition. Electrodeposition is an inexpensive method to produce nanomaterials due to the fact that it does not use vacuum or high temperature. Electrochemical deposition is a promising method to obtain CoSb$_3$ (doped and undoped) nanomaterials at low temperature using template synthesis. Compared to other

These are not the final page numbers! ↗↗

methods, electrodeposition is one of the most cost-effective techniques for the fabrication of nanostructured materials. The advantages of electrodeposition include: room temperature operation, thus reducing problems with thermal stress; low equipment cost; no vacuum requirement; high deposition rates; and easy scalability [17].

Several authors have been used electrochemical deposition to develop $CoSb_3$. Complex tartrate and citrates baths have been used for Sb deposition mainly because of its low solubility in aqueous solutions [18]. Sadana et al. [19] used citrate ions to electrodeposit Sb-Co alloys from aqueous solutions. Using citrate complexes of the two metals brings their deposition potentials closer. Cheng et al. [20] obtained Co-Sb thin films on stainless steel substrates using citric-based solutions. Previous work also reported the growth of Co-Sb nanorods in citrate solution using polycarbonate track-etched (PCTE) templates [21]. Behnke et al. [22] investigated the post-deposition annealing treatment of Co-Sb nanowires to form $CoSb_3$ and reported certain difficulties in obtaining a good stoichiometry due to the antimony loss during heat treatment. Chen et al. [23] found that $CoSb_3$ nanowires with a preferred [420] and [510] orientation could be formed directly at room temperature by electrodeposition of Co and Sb from a tartaric acid solution. Our group [21b,24] has also performed extensive electrochemical studies to understand the co-deposition of Co–Sb on Au substrate as both ultra-thin film and nanowires.

The aim of this work is the study the co-deposition processes of Te-doped $CoSb_3$ and Ni-doped $CoSb_3$ thin film and nanowire to achieve a better understanding of the deposition mechanism and deposition rate of individual elements and how they interact during co-deposition. A comprehensive analysis of the electrochemical processes, including hydrogen evolution, on the finial composition, structure and morphology of the final deposit have been also studied.

2. Experimental Procedure

Electrochemical experiments were performed in a conventional three-electrode set up. The counter electrode was an Au wire and the reference electrode was Ag/AgCl electrode (3 M NaCl). All potentials are relative to Ag/AgCl (+0.210 V vs standard hydrogen electrode). A computer-controlled potentiostatic (model AFCBP1, Pine Instrument Company) was used for cyclic voltammetry, deposition-stripping experiments and potentiostatic cathodic electrodeposition. The Aftermath software (National Instruments, TX, USA) was used to control the potentiostat.

Gold sputtered polycarbonate track-etched (PCTE) membranes (GE Water & Process Technologies, PA, USA) were used as substrates for deposition. The PCTE template is 10 μm thick, and the pore diameters are approximately 400 nm in average. One side of the PCTE
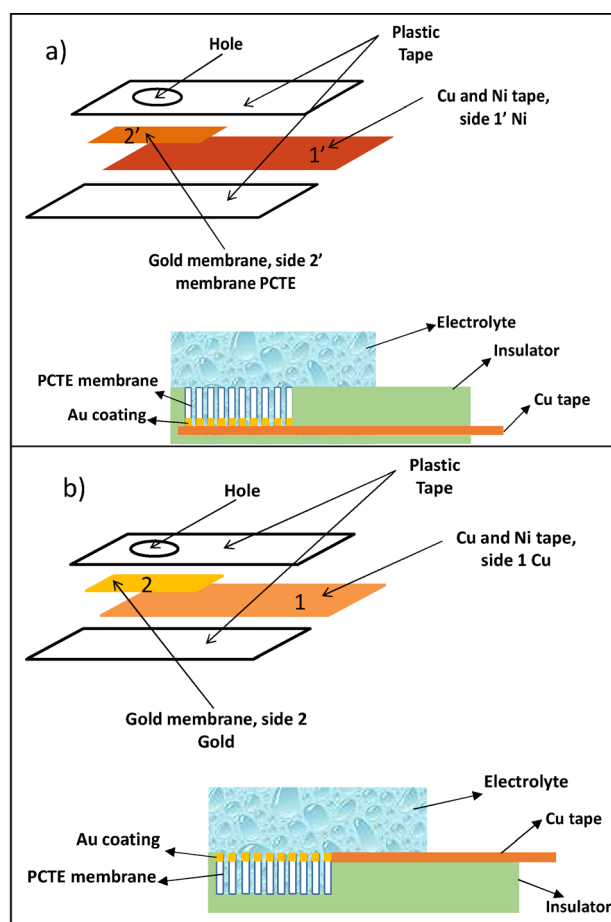

Fig. 2. Schematic 3D (left) and cross section (right) set up working electrode for a) nanowire and b) film configuration.

membranes was sputtered with Au. The area occupied by the pores for the 400 nm membranes was 12.57%.

An Au-coated, PCTE template was then placed on a copper tape and mounted in between two plastic tapes, one of them with a circular cut-out, exposing either the Au coated side for thin film deposition or the uncoated side of the PCTE membrane for nanowire growth. In the case of nanowire growth, the Au-coated PCTE membrane was first immersed in n-butanol solution for 20 seconds to wet the membrane pore, rinse with aqueous electrolyte (see below) and then the template was mounted. The circular cut-out had an area of 0.3846 cm^2. Figure 2 shows the schematic sample setup configuration of the two working electrodes: a) nanowire and b) film. Thin film deposition was performed on the nanostructured Au surface while nanowires were grown in the pores of the PCTE template.

The electrochemistry experiments and the electro-deposition were performed in aqueous electrolyte solutions containing the chemicals of interest, Sb_2O_3 (99.99%), $CoSO_4 \cdot 7H_2O$ (>99%), $C_6H_7KO_7$ (potassium citrate monobasic) (>99.5), $C_6H_8O_7$ (citric acid) (>99.5%) and TeO_2 (99.995%). All the chemicals were purchased from Sigma-Aldrich.

Table 1. Composition of different citrate solutions

Solution	Description
(1)	0.125 M C6H7KO7 + 0.196 M C6H8O7
(2)	0.125 M C6H7KO7 + 0.196 M C6H8O7 + 0.003 M Sb2O3
(3)	0.125 M C6H7KO7 + 0.196 M C6H8O7 + 0.172 M CoSO4
(4)	0.125 M C6H7KO7 + 0.196 M C6H8O7 + 0.001 M TeO2
(5)	0.125 M C6H7KO7 + 0.196 M C6H8O7 + 0.005 M TeO2
(6)	0.125 M C6H7KO7 + 0.196 M C6H8O7 + 0.172 M NiSO4
(7)	0.125 M C6H7KO7 + 0.196 M C6H8O7 + 0.003 M Sb2O3 + 0.172 M CoSO4
(8)	0.125 M C6H7KO7 + 0.196 M C6H8O7 + 0.003 M Sb2O3 + 0.170 M CoSO4 + 0.002 M NiSO4
(9)	0.125 M C6H7KO7 + 0.196 M C6H8O7 + 2.97 mM Sb2O3 + 0.172 M CoSO4 + 0.03 mM TeO2

Table 2. Deposition – stripping experiments

Solution	Deposition Condition Potential vs Ag/AgCl/ Time	Stripping Condition Potential vs Ag/AgCl/ Time
Solution 1	−0.10−−1.00 V/5 min.	N/A
Solution 2	−0.10−−1.20 V/10 min.	0 V/10 min.
Solution 3	−0.30−−1.20 V/5 min.	−0.2 V/5 min.
Solution 4	−0.10−−0.90 V/5 min.	+0.5 V/5 min.
Solution 5	−0.25−−0.60 V/5 min.	+0.5 V/5–15 min.
Solution 6	−0.55−−1.20 V/5 min	+0.4 V/5 min

Various aqueous solutions were prepared with different concentrations as shown in Table 1. Each citrate solutions contained one of the elements of interest, as well as a combination of ions. For instance, solutions 8 and 9 contain beside Co and Sb, and 1% Ni and 1% Te, respectively. Deionized water (Milli Q 18-MΩ) was used for preparing solutions and for rinsing. All solutions were stirred and heated up to 60 °C for at least 45 min (or 12 h in the case of citrates with 0.005M TeO_2) until all chemicals were dissolved. Solutions were purged with N_2 for at least 15 min before experiments to remove oxygen dissolved in the electrolyte solution.

Before electrodeposition, an electrochemical treatment of the Au surface was performed to clean the surface and to ensure reproducible results during the electrochemical studies [25]. This treatment consists of cleaning the surface by cycling the potential between 0 to 1.5 V for 20 times followed by an electrochemical annealing 20 min at 0.9 V. The electrochemical treatment is carried out in 50 mM H_2SO_4 aqueous solution at room temperature.

Electrodeposition of Co, Ni, Te and Sb in citrate solutions is often performed at potentials more negative than −0.9 V vs. Ag/AgCl where the hydrogen evolution reaction (HER) is quite significant. In this potential range, it is difficult to study the deposition rates of these elements due to the fact that hydrogen evolution overlaps with the metal deposition. Therefore, the stripping process was used to study the metal deposition. To achieve this objective, individual deposition-stripping experiments have been carried out for Co, Sb, Te and Ni. Table 2 summarizes deposition – stripping experiments (i.e. potential and time) in a given solution.

Deposition-stripping experiments were performed for each element of interest in its own solution to determine their deposition rates. Deposition was carried out at different potentials between −0.2 and −1.2 V for 5 min followed by stripping. In the case of Solution 2 and 5, the stripping time was increase to 10 and 15 min due to the fact that we observed experimentally a slow removal of Sb and Te, respectively. Solutions were stirred with a mag-

netic stirrer at a rate of 500 rpm. Hydrogen evolution, which is associated with metal deposition at negative potentials, was also studied.

Structural characterization was performed using a high resolution scanning electronic microscope (SEM) with energy dispersive X-ray spectroscopy (EDS) capability. XRD experiments were carried out in order to study the influence of the electrochemical treatment on the gold surface as the working electrode.

3. Results and Discussion

3.1. Electrochemical treatment of the Au surface

A series of electrochemical treatments were performed in 50 mM H_2SO_4 in order to clean the Au surface and to ensure same surface conditions before each electrodeposition experiment [25a–c]. First, 10 CV cycles were performed from 0 to 1.5 V at a sweep rate of 50 mV/s, followed by an electrochemical annealing treatment that was carried out at 0.9 V for 15 minutes (Figure 3).

Figure 4 shows the cyclic voltammetry of the Au surface in 50 mM H_2SO_4 at a sweep rate of 50 mV/s in all three preparation states: first CV on the initial Au surface, before any treatment is applied to the surface (1st cycle), the CV of Au after 10 CV cycles between 0 and 1.5 V (10th cycle) and the CV of Au recorded after holding the potential at 0.9 V for 20 min (after annealing).
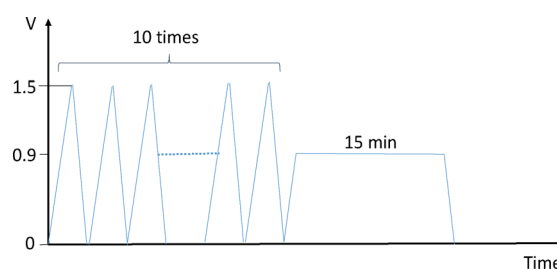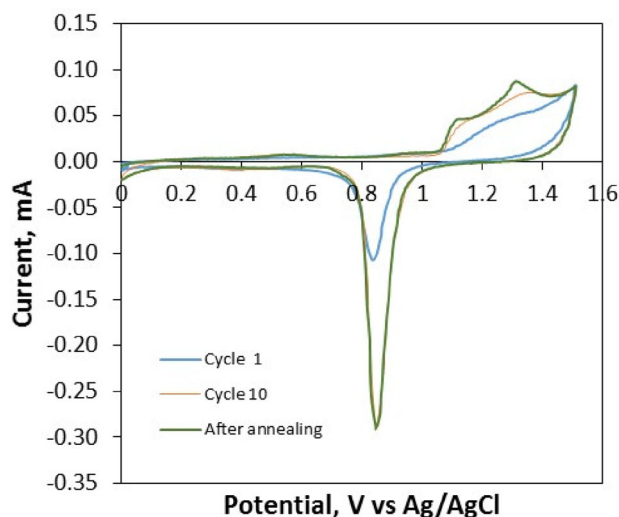

Fig. 3. Au surface treatment steps.

Fig. 4. Cyclic voltammetry of the Au layer on 400 nm PCTE membrane in 50 mM H_2SO_4, v = 50 mV/s: initial CV, before any tratment is applied to the surface, CV recorded after 10 CV cycles between 0 V and 1.5 V, and CV recorded after holding the potential at 0.9 V for 15 min.

Fig. 5. XRD analysis on film and nanowire set-up electrodes before and after cleaning

Figure 4 shows that although the position of Au oxidation peaks for the initial surface indicates a polycrystalline Au surface with no defined oxidation peaks, the peak around 1.3 V becomes predominant, shifts to about 1.2 V, and becomes sharper during the electrochemical treatment The configuration of the Au oxidation curve points to a potential-dependent rearrangement of the Au atoms in the surface during the electrochemical annealing, which is due to high surface diffusion of Au atoms under the applied potential [24–25, 26].

During the electrochemical treatment, the Au surface atoms rearrange themselves by surface diffusion, and this process results in improved surface quality and experimental reproducibility. A change in surface roughness has a distinct signature in the CV by the peak shift. However, it is difficult to estimate from the CV alone which Au plane predominantly smoothers out during annealing. Because the Au film used as an electrode has a nanostructured morphology induced by the open-pore PCTE membrane, the interface processes will be affected compared to a smooth surface. A nanostructured surface has a roughness that changes the structure of the double layer at the interface and interferes with the oxidation process [27]. Therefore, to assess the influence of the electrochemical annealing on the nanostructured Au substrate, an extensive XRD analysis was performed on both film and nanowire setup electrodes before and after the electrochemical treatment. Figure 5 shows the XRD results recorded in the 2θ interval from 36 to 42 degrees, where a change in the XRD peak of Au(111) was observed.

To quantify the structural changes induced by the electrochemical treatment of the Au surface, the crystalline size was calculated using the Scherer equation as follows:
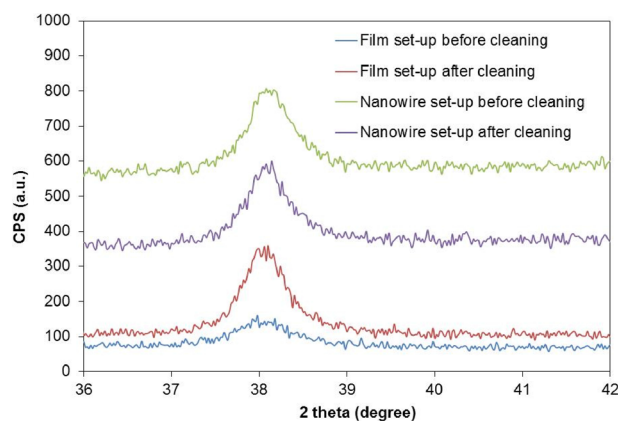
$$\sigma = \frac{k\lambda}{\beta \cos\theta} \tag{2}$$

where σ is the size of the ordered domains, κ the dimensionless shape factor with a value close to the unity (the shape factor has a typically value of about 0.9), λ is the X-ray wavelength, β is the line broadening at half the maximum intensity (FWHM) after subtracting the instrumental line broadening in radians, and θ is the Bragg angle. XRD analysis of Au surface before and after treatment shows a distinct difference in grain size. After EC annealing, the grain size increased from 9.6 to 11.6 nm for the Au film set-up and from 8.1 to 8.6 for the Au nanowire set-up. These results demonstrate the high surface diffusion of Au atoms at 0.9 V, which is at the positive end of the non-faradaic region of Au in 50 mM H_2SO_4. The difference in grain size between the nanowire and film setup electrodes may be related to the direction of Au sputtering on the PCTE membrane, which is perpendicular to the surface (in the film setup) and at an angle in the pores (in the nanowire set-up). Therefore, the Au surface exposed to the electrochemical field during the EC treatment has different orientations in the two sample setups, which affects the direction in which the smoothing develops.

The increase in Au(111) grain size demonstrates the effectiveness of this process induced by surface diffusion. These results are in agreement with the studies performed in situ at the electrode/electrolyte interface. Hirai [26e] investigated by electrochemical atomic force microscopy (ECAFM) the surface self-diffusion coefficient (D(s)) on Ag(100) and Au(100) in aqueous 50 mM H_2SO_4 solution. The surface diffusion increases exponentially with potential in the most positive end of the non-faradaic region. The high surface diffusion of Au atoms is due to the surface excess charge that decreases the activation energy of surface diffusion. High surface diffusion means high surface atomic mobility that results in a smooth surface. The smoothing process starts by the migration of the top atoms down to a lower terrace position. This smoothing

mechanism by atom diffusion has been observed by in situ electrochemical atomic force microscopy (EC-AFM), which is one of the techniques that allow imaging the surface with atomic resolution. Using this technique in liquid, under potential control, the surface atomic diffusion was demonstrated by the disappearance of top terraces and the enlargement of the lower terraces [26d]. The rate of surface atoms mobility expressed as the decay of the top terrace area decreases linearly with time. The mobility of surface atoms in liquid is about 30 times higher than in air. In liquid, the presence of excess charge and electric double layer may increase the atom instability atop the electrode at the metal/electrolyte interface resulting in smoothing of the electrode surface.

These results point to a unique way to improve the smoothness of the surface at atomic level in less than 30 minutes. Other interesting processes such as electrochemical atomic layer epitaxy (ECALE) and surface alloying may take advantage of this fast electrochemical annealing process [25a–d, 28].

3.2. Cyclic Voltammetry

In order to better understand the electrochemical co-deposition and doping, cyclic voltammetry was recorded for Au in Co-Sb solutions containing nickel and tellurium, and compared to those obtained in Co-Ni solution. Figure 6 shows the cyclic voltammograms of Au in solution 8 (Co, Ni and Sb) and 9 (Co, Sb and Te), and compared to solution 7 that contains only Co and Sb. Cyclic voltammograms were recorded at a sweep rate of 5 mV/s from −1.2 V to 0.5 V and 0.7 V (for solution containing Te ions).

Cyclic voltammograms of Au in Co-Sb and (Co, Ni)-Sb show two oxidation peaks and no clear reduction peak. Electrochemical deposition of Co and Sb from their solutions was already published by our group [21b, 24]. Hydrogen evolution is significant for this system and may overlap the deposition peak(s). Adding Ni-ions in the electrolyte does not visibly affect the CV. Ni and Co form solid solutions over the entire concentration range [29] and this may be the reason why the two CVs are similar. Unlike Ni, the addition of Te ions drastically changes the
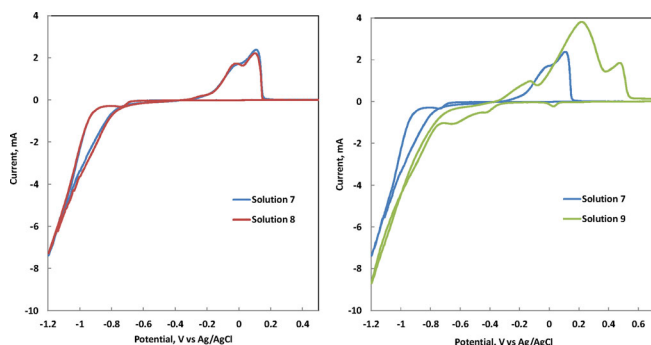
CV, i.e. additional deposition and stripping peaks appear. The potential range for CV in Te- containing Co-Sb solution was extended in the positive direction from 0.5 to 0.7 V to allow for the deposit to be removed from the surface during stripping. As Figure 6 shows for solution 9, stripping currents are much larger compared to solution 7 and shift to more positives values, suggesting a more complex deposition process in the presence of Te-ions. Surface alloying [28b] is one of the processes that may be responsible for the potential shift, since the deposited atoms that interacted with the substrate require an energy to break free from the substrate larger than in the absence of such interactions.

Also, by comparison, Te has a significant impact on the deposition of Co-Sb compared to Ni.

3.3. Deposition-stripping experiments

Deposition-stripping experiments were conducted on the nanostructured Au film to assess the deposition rate of each element of interest, i.e. Co, Sb, Ni, and Te in their individual solutions according to Table 2. Figure 7 shows a typical plot of the current recorded during the deposition performed at a given potential within −0.55 and −1.2 V, and the current recorded during the stripping performed at 0.4 V i.e. the potential where stripping of the entire deposit is concluded [24]. In Figure 7, a negative current indicates a reduction (deposition) process at the working electrode while a positive value means oxidation (stripping).

Electrochemical deposition starts with a very short period of nucleation followed by growth, as indicated by a sharp increase in current followed by stabilization. At the negative end of the potential scanned, the total current is a combination of charge transfer due to both hydrogen evolution and material deposition. During stripping, the current increases rapidly until it reaches a maximum value, as the material that was deposited is removed, and then the current drops to zero.

Fig. 6. Cyclic voltammetry of Au in Co-Sb solution and Ni (left) and Te-ion (right) containing Co-Sb solution at 5 mV/s.
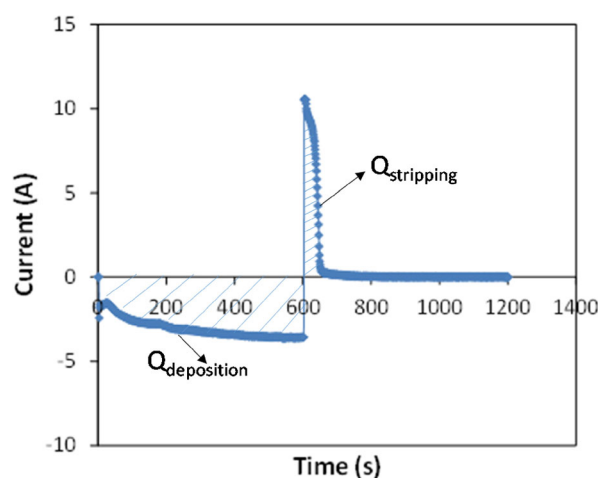

Fig. 7. Current evolution during a deposition-stripping experiment at a certain potential.

In the absence of hydrogen evolution, the two charges associated with deposition and stripping should be equal. Obviously, $Q_{deposition} > Q_{stripping}$ due to hydrogen co-deposition with each metal. In any occurrence, the total charge associated with stripping should reflect the amount of metal deposited since hydrogen will eventually evolve and not strip. Therefore, the area under the I-t stripping curve ($Q_{stripping}$) corresponds to the total charge transferred during metal deposition. Using Faraday's Law (eq. 3), the amount of the material deposited at a certain potential can be calculated from the charge measured during stripping, as follows:

$$m = \frac{Q \cdot M}{F \cdot z} \tag{3}$$

where m is the mass of the material removed during the stripping period, M is its molecular weight, F is Faraday's constant (96,485 C/mol) and z is the valence, which in this case is $z = 2$ for Co and Ni, 3 for Sb and 4 for Te. Since the amount of the material removed during stripping is equal to the amount of solid materials deposited, the average deposition rate or current density, of solid materials can be calculated as follows:

$$Q = i \cdot t \tag{4}$$

where i is the current density (mA/cm^2) and t is the time (s).

Figure 8a) shows the current density due to the deposition of Co, Ni, Sb and Te in their respective citrate solutions, i.e. solution 2, 3, 4 and 5. The deposition of Te does not start until the potential is more negative than −0.3 V. Te deposition rate increases quickly as the potential reaches about −0.45 V, and then remains constant. Results show that when Te was deposited at a potential more negative than −0.6 V, the Te film could not be completely stripped off even when the stripping potential was increased from +0.5 to +0.7 V and held for a more than 10 minutes. Since the stripping data directly affects the calculation of current density during deposition, only results from −0.2 to −0.6 V are shown in Figure 8a).

For Sb, the deposition starts around −0.65 V and increases quickly as the deposition potential reached −0.8 V. For potentials more negative than −0.8 V, the current density for Sb did not change much and the current stabilized around 2.58 mA/cm^2.

The deposition of Co in a citrate solution containing 0.172 M CoSO$_4$ started around −0.85 V. The deposition current steadily increases as the deposition potential becomes more negative. Same results were observed for Ni, Figure 8b). The electrodeposition of Ni starts at potentials more positive than Co but more negative than Sb or Te. The main difference between Ni and the other elements is that the current density is much smaller than the current density obtained for Co, Sb and Te. Because the current densities for Ni deposition are much lower compared
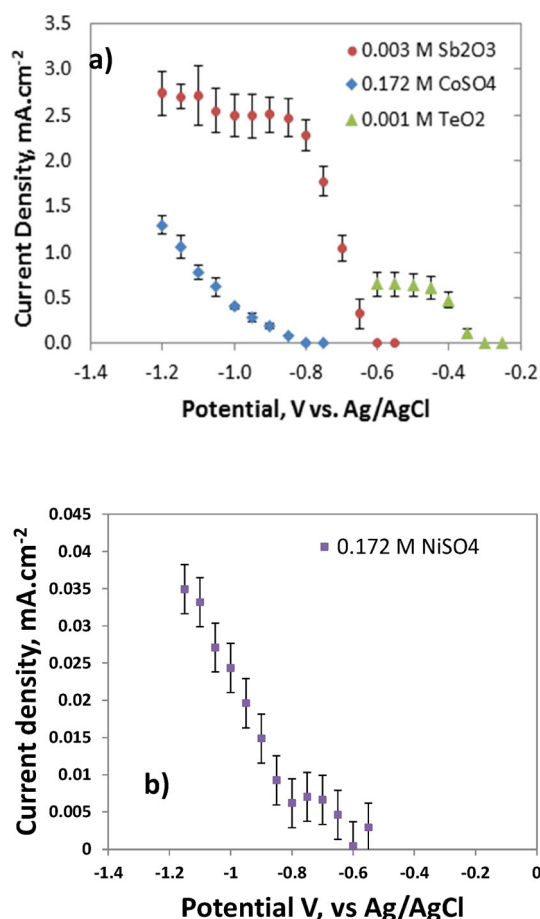

Fig. 8. Deposition rates of Co, Sb, Te, a) and Ni b) in their respective citrate solutions

to Co, Sb or Te, the results for Ni are shown in a separate chart.

In the potential range used in this study, the deposition of Co appears to follow the Butler-Volmer equation (equation 5 [30]), and increases with the overpotential increase:

$$i = i_0 \left[e^{\frac{(1-\beta)\eta F}{RT}} - e^{\frac{\beta \eta F}{RT}} \right] \tag{5}$$

where i is the deposition current, i_0 is the equilibrium exchange current, β is the symmetry factor, η is the overpotential, F is the Faraday's constant, R is the ideal gas constant and T is the temperature.

Although the Butler-Volmer equation predicts an increase in the magnitude of the deposition current with overpotential, the reaction rate cannot increase indefinitely with the applied potential because at some point, the diffusion of cations or complexes containing depositing cations cannot keep up with the reduction reaction at the electrode. When that instance occurs, the deposition rate is constrained by the diffusion of cations/depositing species and is independent of the deposition potential or
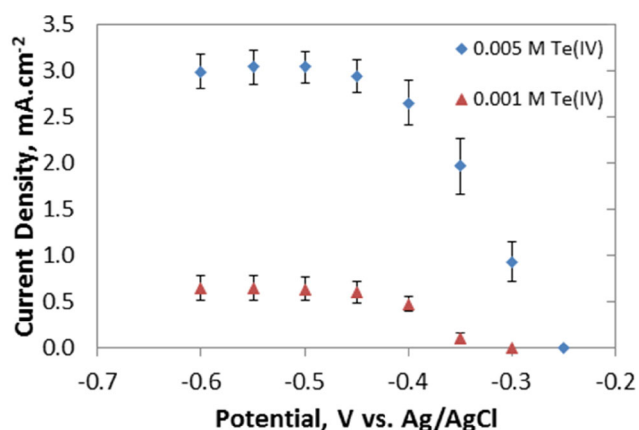
Fig. 9. Effect of the concentration of Te (IV) in citrate solution on its current density during deposition at different potentials.

overpotential. In this case, the limiting current (i_L) is described as [30]:

$$i_L = \frac{z \cdot D \cdot F \cdot C^0}{\delta} \qquad (6)$$

where z is the valence, D is the diffusion coefficient of the cation, δ is diffusion length, F is the Faraday's constant and C^0 is the concentration of the cation in the electrolyte far away from cathode.

At a given temperature and concentration, the deposition current cannot be greater than the limiting current. This behavior can be seen in Figure 8.a) where the current density for Te and Sb remains constant at a large overpotential, which means that Sb and Te deposition are controlled by diffusion.

To study the influence of the concentration on the electrodeposition of Te, we have carried out deposition/stripping experiments for Te in two different citric solutions with different Te concentration, i.e. 0.005 M and 0.001 M TeO_2 (solution 5 and 4 respectively, Table 1). If we apply the Faraday's law to these experiments, the amount of the material deposited and thus the current density can be obtained. Figure 9 shows the current density obtained during the deposition of Te from solutions 4 and 5. The difference between these two solutions is the nominal concentration of Te (IV), which is 0.001 M in solution 4 and 0.005 M in solution 5. The amount of Te (IV) in the solutions is negligible as compared to 0.196 M of citric acid and 0.125 M of potassium citrate, which brings the pH to approximately 2.17. The solid solubility limit of Sb_2O_3 and TeO_2 in simple acid solution such as sulfuric acid is a function of pH and it is about 10^{-4} M for Sb_2O_3 and about 10^{-5} M for TeO_2 at pH=2.75 [31]. These oxides can best dissolve in acidic solution of citrate, tartrate etc. due to the formation of stable complexes, and when this occurs, almost all of Sb (III) and Te (IV) nest in complexes.

Recently, the reduction of Sb (III) in tartaric acid solution was studied by Li [32] who found that the vast majority of the deposit came from the reduction of Sb (III) complex. Similarly, since almost all Te (IV) is in a complex form, the limiting current for Te is bound to the diffusion of Te (IV) complex in the electrolyte to the cathode. A five-time increase in the concentration of Te (IV) complex in solution 5 is the cause of an approximately five-time increase in its limiting current densities at potentials more negative than −0.4 V as observed in Figure 9).

As demonstrated in Figure 8a, the limiting currents for Sb and Te can be easily observed in the range of potentials investigated in this study. This is due to the low concentrations of Sb (III) 0.006 M and Te (IV) 0.001 M. On the other hand, the deposition of Co or Ni has not reached its maximum value, for the total concentration of electroactive species containing Co (II) or Ni (II) is high, i.e. 0.172 M, as compared to those for Sb(III) and Te (IV). Using the limiting current densities for Sb and Te in Figure 8a and equation 6, the diffusion coefficients of Sb(III) complex and Te (IV) complex that control the deposition rate can be calculated. Since antimony and tellurium have the same size, we can assume that the diffusion lengths for Sb and Te are similar, i.e. $\delta_{Sb} \approx \delta_{Te} \approx 10^{-3}$ cm [33], thus we obtain $D_{Sb(III)} \approx 1.5 \ 10^{-6}$ cm^2/s and $D_{Te(IV)} \approx 1.7 \ 10^{-6}$ cm^2/s at 22 °C. The diffusion coefficient for Te(IV) citrate complex found in this study is smaller than the value for $HTeO_2^+$ ($2 \ 10^{-5}$ cm^2/s) in a sulfuric acid solution (pH=1.5) at 60 °C with no complex formation.[33] The difference is probably due to higher temperature used by Sella *et al.* [33] and to the various forms of electroactive species containing Te (IV) citrate complex used. The diffusion coefficient of Te(IV) citrate complex found in our study is similar to that reported by Jung *et al.* [34] (i. e. $3.1 \ 10^{-6}$ cm^2/s at 23 °C) in a nitrate-tartrate solution.

3.4. Hydrogen Evolution

Hydrogen evolution was studied by subtracting the charges associated with metal deposition (i.e. from stripping data) from the total charges transferred during deposition process. Figure 10 shows the variation of the current for hydrogen deposition with the applied potential for various solutions citrates (solution 1), citrates+0.003 M Sb_2O_3 (solution 2), citrates+0.172 M $CoSO_4$ (solution 3), citrates+0.001 M Te (solution 4) and Citrate+0.172 M $NiSO_4$ (solution 6). Charges transferred due to hydrogen evolution were calculated by subtracting the partial charges transferred due to stripping of a given element from the total charges measured during deposition experiments.

For all the solutions studied, hydrogen evolution is not significant for potentials more positive than −0.65 V. For solution 1, in the absence of any metal ion, hydrogen evolution is the only reaction occurring at Au surface. For all other solutions, hydrogen evolution curves overlaps up to −0.7 V with that obtained in the solution containing only citrates. At potentials more negative than −0.7 V, hydrogen evolution occurs on different substrates since the
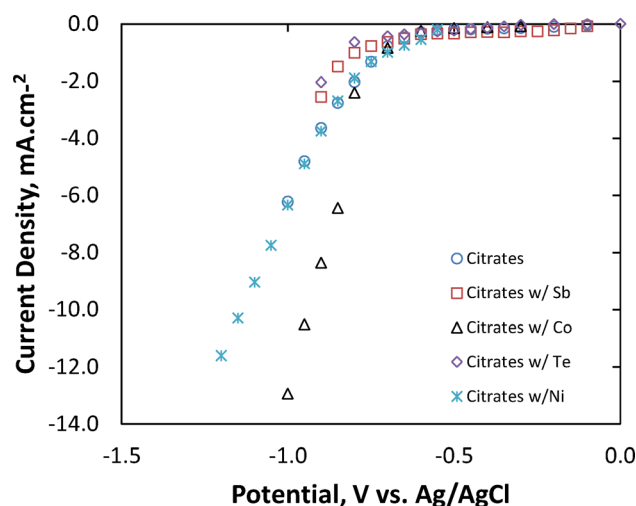
These are not the final page numbers! ↗↗

Fig. 10. Hydrogen evolution in different citrate solutions.

Fig. 11. SEM images of Co-Sb film (a), nanowires array (b), and mushroom cups (c) in solution 7 at a constant potential of −1 V.

onset potential for Sb and Te deposition overlaps with hydrogen evolution. At these negative potentials, hydrogen evolution does not take place on Au but on Sb (see Figure 8).

At more negative potential, hydrogen evolution is significant high for solutions that contain either Co or Ni because their deposition takes place at potential close to −0.9 V. Compared to Au substrate, the results presented in Figure 10 suggest that the presence of Sb and Te suppresses hydrogen evolution while Co and Ni enhances it. These findings are consistent with literature data for hydrogen evolution from simple acidic solutions on different substrates such as Au, Co, Ni, Sb and Te [31]. The current density for hydrogen evolution on each substrate is related to the binding energy between the substrate and hydrogen atoms [32].

3.5. Morphology and Composition of Co-Sb Film and Nanowires

Once the kinetic of the electrodeposition of undoped $CoSb_3$ and doped with Te and Ni has been studied, a study of the morphology and composition of the material obtained has been carried out. To achieve this objective a detailed investigation of the morphology and composition of Co-Sb thin films and nanowires was performed using SEM and EDS. Deposition experiments have been performed in citrate solution 7 containing both 0.172 M Co(II) and 0.006 M Sb(III) and the potential for these experiments was −1 V.

Figure 11 shows the SEM images for Co-Sb film, nanowire and mushroom cups (i.e. overgrown nanowires).The film is relatively uniform and deposits on the entire membrane surface (Figure 11a), including the pores. Local variations in morphology may be associated with the particular nature of the nanostructured Au surface and hydrogen evolution [24]. Figure 11b shows a typical nanowire array grown in a template. Generally, the formation of nano-
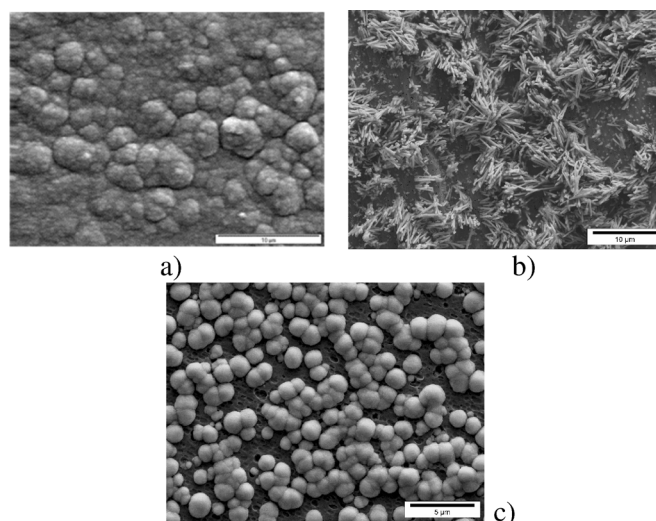
wires inside a template takes place by means of a nucleation and growth process in several steps [24]. The first process corresponds to a nucleation and growth of the nuclei inside the pores. The nucleation process starts at the bottom of the pores where the Au ring acts as an electrode. These nuclei grow freely in both radial and axial directions inside the template to a point where the nuclei start to overlap in the radial direction. The second step is a continuous growth of nuclei, which overlap inside the template. The third step is related to "mushroom" formation, where the nanowires continue to grow out and over the template. The last step is characterized by a rather constant, radial, growth of a film that bridges the mushrooms. The film is relatively uniform and deposits on the entire membrane surface including pores. Local variations in morphology may be associated with the particular nature of the nanostructured Au surface and possible hydrogen evolution.

Figure 12 shows the variation of the Co amount in the deposit with the potential applied for different structures, film, nanowires and mushrooms. An illustration of the structures on which the composition was measured is also shown.

For films, three different sets of data are plotted. One set consists of the EDS results obtained for films deposited in citrate solution 7 containing both 0.172 M Co(II) and 0.006 M Sb(III). Another set of data shows the atomic % of Co in the deposit as calculated using Faraday's Law (eq. 3) for citrate solution containing both 0.172 M Co(II) and 0.006 M Sb(III), where the Co and Sb deposition rates measured from their respective individual solutions (Figure 8) were used. The third set of data shows the experimental results obtained by Cheng [20,35] in similar solutions, i.e. same Co concentration and half the concentration of Sb. These plots show good agreement between the literature and experimental data and
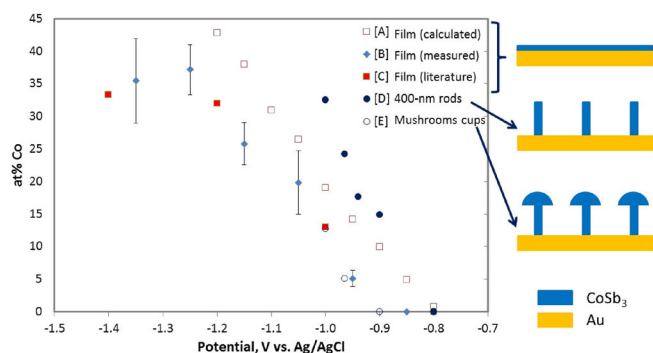
Fig. 12. composition of Co deposited from citrate solution with 0.172 M Co (II) and 0.006 M Sb (III): a) film calculated based on single solutions of Co (II) and Sb (III), b) film experimental results in solution of both Co (II) and Sb (III), c) film results from Cheng [20], d) 400 nm rods from Quach [24], and e) mushroom cups from Quach [24].

a similar increase of Co content in the deposit as the deposition potential become more negative. At potentials more negative than −1.2 V, experimental data indicate a lower content of Co as compared to those calculated from single solutions.

These results might be explained by taking into consideration the deposition rates of Co and Sb in their respective citrate solutions (Figure 8). Analyzing the deposition rates of Sb, it appears that the deposition of Sb at potentials more negative than −0.8 V is controlled by diffusion while the rate of Co deposition depends on its electrode reaction. Therefore, it is believed that the deposition of Co is more sensitive to the cathode's surface condition, and the rate at which Co deposit is reduced in the presence of Sb on the electrode surface. Although there are other compounds that may form between Co and Sb, such as CoSb and CoSb$_2$, only CoSb$_3$ is favorable at room temperature due to its negative Gibbs free energy. Therefore, a reduced deposition rate of Co in the presence of Sb is probably due to a larger kinetic barrier.

For comparison, the composition data of nanowires and overgrown mushroom caps from previous works performed in our group [24] are also shown. Interestingly, Co content in 400 nm nanowires is higher than in the film or the calculations. Because all the deposition experiments were performed in stirred solutions at a rate of 500 rpm, the convection of electrolyte the may not be very effective to improve the diffusion of species in nanopores. As discussed earlier, deposition of Sb below −0.8 V is controlled by diffusion. Therefore, the diffusion of Sb complex through the pores may be slower, which directly impacts the relative content of Co in the deposit. Overgrown mushroom caps have a composition similar to films, and the Co content follows the same trend as that of the film as shown in Figure 12.

3.6. Morphology and Composition of doped Co-Sb Film and Nanowires

Structural and compositional characterization of Ni and Te doped Co-Sb nanowires obtained from the solutions 8 and 9 were performed using SEM/EDS. Ni-doped and Te-doped nanowires were obtained by pulse electrodeposition (−0.965/−0.4 V, 10/10 ms) at 65 °C to improve compositional homogeneity of nanowires.

Figure 13 shows the SEM images of Te-doped and Ni-doped Co-Sb nanowires. In this particular case, electrochemical doping is realized by co-deposition of Co-Ni-Sb and Co-Sb-Te in a template. It appears that doping does not affect the nanowire morphology or structural sturdiness.

Table 3 presents the composition of Ni and Te-doped nanowires in comparison with Co-Sb nanowires. To assess the dopant contribution to nanowire composition, the ratio of (Co, Ni) to (SbTe) was calculated and presented in table 3 along with the nanowire composition. It appears that adding Ni ions in the solution results in a slight increase of the (Co, Ni)/(SbTe) ratio while adding Te ions results in a decrease of the (Co, Ni)/(SbTe) ratio. It is important to note that the total molarity of the Co-Sb solution was not changed by adding Ni or Te (see Table 1) but only the composition of the electrolyte.

Electrochemical doping of Co-Sb requires additional study. For instance, Co-Ni shows anomalous deposition that may affect the Co/Ni ratio in the deposit. Dolati et al. [36] studied the composition of electrodeposited Co-Ni alloy nanowires for Co^{2+} concentrations ranging from 0.1 to 0.2 M at constant Ni^{2+} concentration and showed that there is a direct relationship between the solution concentration and nanowire concentration. They also studied the variation of the Co concentration in the deposit with the applied voltage and showed that there is
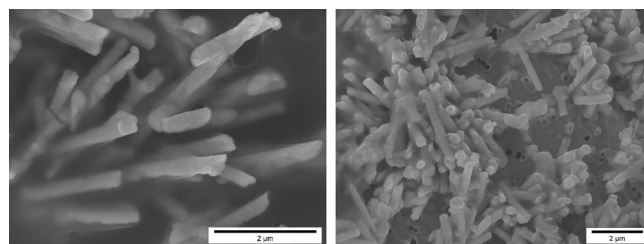

Fig. 13. SEM image of Te-doped (a) and Ni-doped (b) Co-Sb nanowires.

Table 3. EDS results obtained for Ni and Te doped nanowires

Composition, at. %	Solution 7	Solution 8	Solution 9
Sb L	1.94 +/− 0.05	1.55 +/− 0.37	3.615 +/− 0.27
Co K	1.87 +/− 0.16	1.61 +/− 0.43	3.34 +/− 0.05
Ni K	–	0.13 +/− 0.09	–
Te K	–	–	0.39 +/− 0.05
(Co, Ni)/(Sb, Te)	0.96 +/− 0.06	1.12 +/− 0.06	0.83 +/− 0.05

a similar direct relationship between the deposit composition and the applied voltage in the low voltage range. At very high voltages, where the deposit growth is diffusion-controlled, the nanowires composition is driven by a competitive diffusion of Co^{2+} and Ni^{2+} that rush to reach in the pore. Therefore, high applied voltages had no effect on the Co composition. However, these findings for Co-Ni nanowires contradict the anomalous deposition behavior observed for thin film electrochemical deposition of Co-Ni [37]. Because the Co concentration in the deposit increases with Co concentration of the solution, Co-Ni nanowires do not show anomalous deposition behavior [37]. However, for low Ni concentrations, more research is needed to rule out the anomalous deposition in nanowires.

4. Conclusions

Electrochemical studies of Co-Sb doped with tellurium and nickel in citric acid solutions have been performed to better understand the electrochemical doping in these systems. The conclusions are as follows:

- Electrochemical annealing: The electrochemical treatment does not only clean the Au surface but also improves its smoothness. XRD studies showed that the gold surface atoms rearranged by surface diffusion during electrochemical annealing and Au(111) domains increased in size.
- Electrochemical deposition/stripping experiments: The results show that the deposition of Co is controlled by the electrochemical reaction at the cathode, while Sb and Te are controlled by diffusion. Although the electrolyte contained citrates that form Sb and Te complexes to increase the solubility of Sb_2O_3 and TeO_2, the deposition of Sb and Te in their citrate solutions is still controlled by diffusion due to their low concentrations. When both Co(II) and Sb(III) are combined in the same citrate solution, their electrochemical behaviors preserve the same characteristics as in single solutions although the relative content of Co is slightly lower. This is probably due to interactions between Co and Sb that give rise to a higher kinetic barrier for the deposition of Co. Deposition of nickel°Ccurs at smaller current densities than other elements and is also controlled by surface reaction.
- Hydrogen evolution: The influence of hydrogen evolution on the co-deposition process is an important issue due to the proximity of their reaction potentials and possible interferences. Hydrogen evolution is significant in the potential window where the co-deposition°Ccurs, being more aggressive on Co surface.
- Composition of the deposit: The co-deposition of Co-Sb results in different compositions depending on the substrate. For instance, the amount of Co is higher in nanowires than in film or mushroom caps due to the slow Sb deposition rate that is limited by Sb(III) complex diffusion. Doped nanowires have been also ob-

tained. Both Ni and Te electrochemical doping of the Co-Sb system affects the composition of the deposit but it has no effect on nanowire morphology.

References

[1] a) T. M. Tritt, M. A. Subramanian, *Mrs Bulletin* **2006**, *31*, 188–198; b) J.-F. Li, Liu, Wei-Shu, Zhao, Li-Dong, Zhou, Min, *NPG Asia Maerials* **2010**, *2*.

[2] H. Anno, K. Matsubara, Y. Notohara, T. Sakakibara, H. Tashiro, *Journal of Applied Physics* **1999**, *86*, 3780–3786.

[3] G. A. Slack, *CRC Handbook of Thermoelectrics*, CRC Press, Boca Raton, FL, **1995**.

[4] a) G. S. Nolas, J. Poon, M. Kanatzidis, *Mrs Bulletin* **2006**, *31*, 199–205; b) K. T. Wojciechowski, *Materials Research Bulletin* **2002**, *37*, 2023–2033.

[5] a) D. T. Morelli, G. P. Meisner, B. X. Chen, S. Q. Hu, C. Uher, *Physical Review B* **1997**, *56*, 7376–7383; b) J. S. Dyck, W. Chen, J. H. Yang, G. P. Meisner, C. Uher, *Physical Review B* **2002**, *65*; c) D. Mandrus, A. Migliori, T. W. Darling, M. F. Hundley, E. J. Peterson, J. D. Thompson, *Physical Review B* **1995**, *52*, 4926–4931; d) X. Shi, W. Zhang, L. D. Chen, J. Yang, *Physical Review Letters* **2005**, *95*; e) E. S. Toberer, M. Christensen, B. B. Iversen, G. J. Snyder, *Physical Review B* **2008**, *77*; f) J. Yang, D. T. Morelli, G. P. Meisner, W. Chen, J. S. Dyck, C. Uher, *Physical Review B* **2002**, *65*; g) J. Yang, G. P. Meisner, D. T. Morelli, C. Uher, *Physical Review B* **2001**, *63*; h) D. J. Singh, W. E. Pickett, *Physical Review B* **1994**, *50*, 11235–11238; i) E. Arushanov, K. Fess, W. Kaefer, C. Kloc, E. Bucher, *Physical Review B* **1997**, *56*, 1911–1917; j) J. Yang, M. G. Endres, G. P. Meisner, *Physical Review B* **2002**, *66*.

[6] a) Q. He, Q. Hao, X. Wang, J. Yang, Y. Lan, X. Yan, B. Yu, Y. Ma, B. Poudel, G. Joshi, D. Wang, G. Chen, Z. Ren, *Journal of Nanoscience and Nanotechnology* **2008**, *8*, 4003–4006; b) M.-J. Kim, S.-C. Ur, I.-H. Kim, *Journal of the Korean Institute of Metals and Materials* **2007**, *45*, 191–194; c) M. Chitroub, F. Besse, H. Scherrer, *Journal of Alloys and Compounds* **2009**, *467*, 31–34.

[7] H. Takizawa, K. Miura, M. Ito, T. Suzuki, T. Endo, *Journal of Alloys and Compounds* **1999**, *282*, 79–83.

[8] J. Jae-Yong, P. Kwan-Ho, K. Il-Ho, *AIP Conference Proceedings* **2011**, *1399*, 31–32.

[9] G. J. Snyder, E. S. Toberer, *Nature Materials* **2008**, *7*, 105–114.

[10] K. Matsubara, T. Sakakibara, Y. Notohara, H. Anno, T. Shimizu, H. Koyanagi, *Proceedings of the 15th International Conference on Thermoelectrics*, Pasadena, CA **1996**, 96.

[11] S. C. Ur, I. H. Kim, *Journal of the Korean Physical Society* **2009**, *55*, 942–946.

[12] K. T. Wojciechowski, J. Tobola, J. Leszczynski, *Journal of Alloys and Compounds* **2003**, *361*, 19–27.

[13] a) L. D. Hicks, M. S. Dresselhaus, *Physical Review B* **1993**, *47*, 12727–12731; b) L. D. Hicks, T. C. Harman, M. S. Dresselhaus, *Applied Physics Letters* **1993**, *63*, 3230–3232.

[14] a) A. I. Boukai, Y. Bunimovich, J. Tahir-Kheli, J.-K. Yu, W. A. Goddard III, J. R. Heath, *Nature* **2008**, *451*, 168–171; b) A. I. Hochbaum, R. Chen, R. D. Delgado, W. Liang, E. C. Garnett, M. Najarian, A. Majumdar, P. Yang, *Nature* **2008**, *451*, 163-U165.

[15] J. C. Caylor, A. M. Stacy, R. Gronsky, T. Sands, *Journal of Applied Physics* **2001**, *89*, 3508–3513.

[16] V. Savchuk, A. Boulouz, S. Chakraborty, J. Schumann, H. Vinzelberg, *Journal of Applied Physics* **2002**, *92*, 5319–5326.

[17] F. Xiao, C. Hangarter, B. Yoo, Y. Rheem, K. H. Lee, N. V. Myung, *Electrochimica Acta* **2008**, *53*, 8103–8117.

[18] Y. N. Sadana, J. P. Singh, R. Kumar, *Surface Technology* **1985**, *24*, 319–353.

[19] Y. N. Sadana, R. Kumar, *Surface Technology* **1980**, *11*, 37–46.

[20] H. Cheng, H. H. Hng, J. Ma, X. J. Xu, *Journal of Materials Research* **2008**, *23*, 3013–3020.

[21] a) D. V. Quach, R. Vidu, J. R. Groza, P. Stroeve, *Industrial and Engineering Chemistry Research* **2010**, *49*, 11385–11392; b) R. Vidu, S. Li, D. V. Quach, P. Stroeve, *Journal of Applied Electrochemistry* **2012**, *42*, 333–339.

[22] J. F. Behnke, A. L. Prieto, A. M. Stacy, T. Sands, *Eighteenth International Conference on Thermoelectrics. Proceedings*, ICT'99 (Cat. No.99TH8407) **1999**, 451–453.

[23] a) L. J. Chen, H. N. Hu, Y. X. Li, G. F. Chen, S. Y. Yu, G. H. Wu, *Chemistry Letters* **2006**, *35*, 170–171; b) L. J. Chen, Y. X. Li, G. F. Chen, H. Y. Liu, X. X. Liu, G. H. Wu, *Chinese Journal of Inorganic Chemistry* **2006**, *22*, 949–951.

[24] D. V. Quach, R. Vidu, J. R. Groza, P. Stroeve, *Industrial & Engineering Chemistry Research* **2010**, *49*, 11385–11392.

[25] a) R. Vidu, S. Hara, *Scripta Materialia* **1999**, *41*, 617–624; b) R. Vidu, S. Hara, *Electrochemistry* **1999**, *67*, 1240–1242; c) R. Vidu, S. Hara, *Journal of Vacuum Science & Technology B* **1999**, *17*, 2423–2430; d) R. Vidu, S. Hara, *Surface Science* **2000**, *452*, 229–238; e) R. Vidu, N. Hirai, S. Hara, *In situ electrochemical atomic force microscopy of surface alloying at the Au(100)/Cd2+ interface*, Vol. 2002, **2003**.

[26] a) N. Hirai, M. Yamauchi, T. Tanaka, S. Hara, *Science and Technology of Advanced Materials* **2004**, *5*, 115–118; b) K. Kubo, N. Hirai, S. Hara, *Applied Surface Science* **2004**, *237*, 301–305; c) N. Hirai, K. Watanabe, S. Hara, *Surface Science* **2001**, *493*, 568–574; d) N. Hirai, K. Watanabe, A. Shiraki, S. Hara, *Journal of Vacuum Science & Technology B* **2000**, *18*, 7–9; e) N. Hirai, H. Tanaka, S. Hara, *Applied Surface Science* **1998**, *130*, 506–511.

[27] S. Dhillon, R. Kant, *Electrochimica Acta* **2014**, *129*, 245–258.

[28] a) N. Ikemiya, D. Iwai, K. Yamada, R. Vidu, S. Hara, *Surface Science* **1996**, *369*, 199–208; b) R. Vidu, S. Hara, *Journal of Electroanalytical Chemistry* **1999**, *475*, 171–180; c) R. Vidu, N. Hirai, S. Hara, *Physical Chemistry Chemical Physics* **2001**, *3*, 3320–3324.

[29] T. Nishizawa, A-B-C Phase Diagram, ASM Alloy Phase Diagrams Database, P. Villars, editor-in-chief; H. Okamoto and K. Cenzual, section editors; ASM International, Materials Park, OH, 2006. **1990**.

[30] J. O. M. B. a. A. K. N. Reddy, *Modern Electrochemistry Vol. 2*, Plenum Press, New York, **1998**.

[31] M. Pourbaix, *Atlas of Electrochemical Equilibria in aqueous Solutions*, NACE, Houston, TX, **1974**.

[32] F.-H. Li, W. Wang, J.-P. Gao, S.-Y. Wang, *Journal of the Electrochemical Society* **2009**, *156*, D84-D91.

[33] C. Sella, P. Boncorps, J. Vedel, *J. Electrochem. Soc.* **1986**, *133*, 2043–2047.

[34] H. Jung, N. V. Myung, *Electrochimica Acta* **2011**, *56*, 5611–5615.

[35] H. Cheng, Hng, H. H. Ma, J. *Solid State Phenomena* **2008**, *136*, 75–82.

[36] A. Ghahremaninezhad, A. Dolati, *Journal of Alloys and Compounds* **2009**, *480*, 275–278.

[37] A. Dolati, M. Sababi, E. Nouri, M. Ghorbani, *Materials Chemistry and Physics* **2007**, *102*, 118–124.
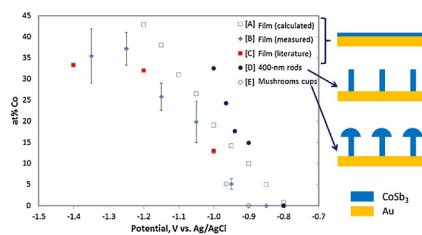
R. Vidu,* M. Perez-Page,
D. V. Quach, X. Y. Chen, P. Stroeve

■■ – ■■

Electrodeposition of Ni and Te−Doped Cobalt Triantimonide in Citrate Solutions